

MICROCOPY RESOLUTION TEST CHART  
NATIONAL BUREAU OF STANDARDS-1963-A

2

AD-A163 736

EXPERIMENTAL STUDY OF THE SUPERSONIC TURBULENT BOUNDARY LAYER  
ON A BLUNTED AXI-SYMMETRIC BODY

FINAL REPORT

D. S. DOLLING

25 OCTOBER 1985

DTIC  
ELECTE  
FEB 07 1986  
S D  
D

U. S. ARMY RESEARCH OFFICE

D A A G 2 9 - 8 4 - M - 0 4 3 2

DEPARTMENT OF AEROSPACE ENGINEERING AND ENGINEERING MECHANICS  
THE UNIVERSITY OF TEXAS AT AUSTIN

APPROVED FOR PUBLIC RELEASE;  
DISTRIBUTION UNLIMITED

DTIC FILE COPY

AD-A163736

REPORT DOCUMENTATION PAGE		READ INSTRUCTIONS BEFORE COMPLETING FORM
1. REPORT NUMBER	2. GOVT ACCESSION NO. N/A	3. RECIPIENT'S CATALOG NUMBER N/A
4. TITLE (and Subtitle) EXPERIMENTAL STUDY OF THE SUPERSONIC TURBULENT BOUNDARY LAYER ON A BLUNTED AXI-SYMMETRIC BODY		5. TYPE OF REPORT & PERIOD COVERED 1 Aug 82 - 31 Jul 85 FINAL
		6. PERFORMING ORG. REPORT NUMBER
7. AUTHOR(s) D. S. DOLLING		8. CONTRACT OR GRANT NUMBER(s) DAAG29-84-M-0432
9. PERFORMING ORGANIZATION NAME AND ADDRESS Department of Aerospace Engineering and Engineering Mechanics The University of Texas at Austin		10. PROGRAM ELEMENT, PROJECT, TASK AREA & WORK UNIT NUMBERS
11. CONTROLLING OFFICE NAME AND ADDRESS U. S. Army Research Office Post Office Box 12211 Research Triangle Park, NC 27709		12. REPORT DATE 30 September 1985
		13. NUMBER OF PAGES
14. MONITORING AGENCY NAME & ADDRESS (if different from Controlling Office)		15. SECURITY CLASS. (of this report) Unclassified
		15a. DECLASSIFICATION/DOWNGRADING SCHEDULE
16. DISTRIBUTION STATEMENT (of this Report)  Approved for public release; distribution unlimited.		
17. DISTRIBUTION STATEMENT (of the abstract entered in Block 20, if different from Report)  NA		
18. SUPPLEMENTARY NOTES  The view, opinions, and/or findings contained in this report are those of the author(s) and should not be construed as an official Department of the Army position, policy, or decision, unless so designated by other documentation.		
19. KEY WORDS (Continue on reverse side if necessary and identify by block number)  Supersonic Turbulent Boundary Layer; Blunt Body Flow, Boundary Layer Velocity Profiles ←		
20. ABSTRACT (Continue on reverse side if necessary and identify by block number)  Surface pressure distributions and turbulent boundary layer velocity profiles have been measured on a tangent-ogive cylinder model at small angles of attack (0-4.5°) in a high Reynolds number, Mach 3 airflow. The model wall temperature was approximately adiabatic. The measurements were made using pointed, tangent-hemisphere and flat-faced nose tips. The effects of tip blunting on the wind- and leeside velocity profiles, integral thicknesses, shape factor, power law exponent, skin friction coefficient and wake strength parameter are presented.		

UNCLASSIFIED

SECURITY CLASSIFICATION OF THIS PAGE(When Data Entered)

20. (continued)

It is shown that the results obtained using different geometry tips can be correlated using a bluntness length-scale obtained by integration of the local tip surface angle from the stagnation point to the point corresponding to shock detachment. — *Figure 19*

UNCLASSIFIED

SECURITY CLASSIFICATION OF THIS PAGE(When Data Entered)

Abstract

Surface pressure distributions and turbulent boundary layer velocity profiles have been measured on a tangent-ogive cylinder model at small angles of attack (0-4.5°) in a high Reynolds number, Mach 3 airflow. The model wall temperature was approximately adiabatic. The measurements were made using pointed, tangent-hemisphere and flat-faced nose tips. The effects of tip blunting on the wind- and leeside velocity profiles, integral thicknesses, shape factor, power law exponent, skin friction coefficient and wake strength parameter are presented. It is shown that the results obtained using different geometry tips can be correlated using a bluntness length-scale obtained by integration of the local tip surface angle from the stagnation point to the point corresponding to shock detachment.

Accession For	
NTIS CRA&I	<input checked="" type="checkbox"/>
DTIC TAB	<input type="checkbox"/>
Unannounced	<input type="checkbox"/>
Justification	
By	
Distribution/	
Availability Codes	
Dist	Avail and/or Special
A-1	



### Nomenclature

- B bluntness length scale (eqn. 1)
- $C_f$  skin friction coefficient
- D cylinder diameter (Fig. 1)
- $Dp_b$  additional drag due to tip blunting
- H shape factor ( =  $\delta^*/\theta$  )
- M Mach number
- n exponent in velocity profile power law
- $P_t$  pitot pressure
- $P_w$  wall pressure
- Re Reynolds number
- S distance along body surface measured from tip
- $u, U$  velocity component in x direction
- X distance along body axis from pointed tip (Fig. 1)
- y distance normal to body surface
- $\alpha$  angle of attack
- $\delta$  boundary layer thickness
- $\delta^*$  boundary layer displacement thickness
- $\theta$  boundary layer momentum thickness
- $\bar{\Lambda}$  wake strength parameter
- $\phi$  circumferential position (Fig. 1)

### Subscripts

- c critical value
- e value at boundary layer edge
- $\infty$  undisturbed freestream

TABLE OF CONTENTS

	<u>Page</u>
<u>Abstract</u> . . . . .	1
<u>Nomenclature</u> . . . . .	11
1. <u>Introduction</u> . . . . .	1
2. <u>Experimental Methods</u> . . . . .	2
2.1 <u>Wind Tunnel</u> . . . . .	2
2.2 <u>Models</u> . . . . .	2
2.3 <u>Angle of Attack</u> . . . . .	2
2.4 <u>Measurements and Data Documentation</u> . . . . .	3
3. <u>Discussion of Results</u> . . . . .	4
3.1 <u>Wall Pressures</u> . . . . .	4
3.2 <u>Boundary Layer Properties</u> . . . . .	5
3.2.1 <u><math>\alpha = 0^\circ</math></u> . . . . .	5
3.2.2 <u><math>\alpha = 2.9^\circ</math></u> . . . . .	7
4. <u>Concluding Remarks</u> . . . . .	9
References . . . . .	10
Publications/Participating Personnel . . . . .	11
Figures . . . . .	12

## 1. Introduction

One of the fundamental objectives of current computational fluid dynamics research is to predict the forces and moments on bodies in high-speed flows. An important class of flows is that over axisymmetric bodies, such as projectiles. A review of present capabilities in this area together with a bibliography of the recent experimental and numerical work has been compiled by Sturek.<sup>1</sup> The reader is referred to it for details. In summary, it is clear that, although many parameters important to designers can now be calculated with acceptable accuracy (at least for simple geometries at small  $\alpha$ ), much remains to be done, particularly with respect to modelling the three-dimensional (3-D) turbulent boundary layer development.

Accurate prediction of the 3-D boundary layer is essential for spin-stabilized bodies where the interaction of the surface spin with the crossflow produces asymmetries in the boundary layer which generate a sideforce (the Magnus force) whose net value is the sum of relatively small pressure and shearing forces (of different sign). Since both components originate in the viscous region, satisfactory predictions of the Magnus force require very accurate modelling of the boundary layer. To evaluate numerical simulation methods, and to understand flow phenomena better, detailed experimental data are needed, both for spinning bodies and for the baseline case of zero spin.

The data base generated over the past decade includes overall aerodynamic coefficients obtained from firing tests and also detailed flow field measurements made in wind tunnels. A large fraction of the wind tunnel studies has used tangent-ogive<sup>2-6</sup> and secant-ogive<sup>7-11</sup> cylinder models, with<sup>5,8-11</sup> and without conical boat-tails. Both spinning<sup>2,4,7,9</sup> and stationary models have been tested. Other than the tests of references 10 and 11 which were made at  $M_\infty = 0.97$  and  $0.94$  respectively, most of the work is in the supersonic regime ( $2 \leq M_\infty \leq 4$ ). The published data are primarily mean flow measurements and include  $P_w$ , profiles of  $P_t$  and  $u/U_e$  versus  $y$ , and  $C_f$ . Other than references 6, 10 and 11, in which tangent-hemisphere and flat nose tips were used, all of the tips tested were pointed. Except in the work of references 2-4, where the tip was pointed but its angle was large enough to cause shock detachment (although the region of mixed flow was very small), the shocks were all attached.

In practice, projectile nose tips are generally blunt and the shock wave is detached. There is some evidence that this may increase the Magnus force.<sup>12</sup> Although the influence of tip bluntness on transition has been studied extensively (i.e., 31 references, including 4 review papers, are cited in the recent work of Stetson<sup>13</sup>), the effects on the subsequent turbulent boundary layer are less well documented. In the current study, surface pressures and boundary layer velocity profiles have been measured on pointed and blunted tangent-ogive cylinder models in a high Reynolds number, Mach 3 airflow. The primary objective was to investigate the influences of tip blunting on the boundary layer properties and provide detailed

data for comparison with numerical work being carried out at the U.S. Army Ballistics Research Laboratory. A description of the experiment and the results are given in this paper. In a follow-up paper, the numerical method and comparisons with experiment will be presented.

## 2. Experimental Methods.

### 2.1 Wind Tunnel.

The experiments were carried out in the Princeton University 20cm. x 20cm. supersonic, high Reynolds number, blowdown tunnel. At the test station, the nominal value of  $M_\infty$  was 2.95. For all tests, the settling chamber conditions were  $P_0 = 6.8 \times 10^5 \text{ Nm}^{-2} \pm 1\%$  and  $T_0 = 265\text{K} \pm 5\%$  respectively, giving a nominal test section  $Re_\infty = 6.3 \times 10^7 \text{ m}^{-1}$ . The model wall temperature was within 3% of the adiabatic value.

### 2.2 Models.

A sketch of the model and coordinate system is shown in Figure 1. Two models were built because there was insufficient internal space to instrument both the cylinder and the ogive-tip section on a single model. Model 1 had the ogive soldered to the cylinder and could be fitted with pointed, flat-faced and tangent-hemisphere nose tips. The tip details and their designations are also given in Figure 1. Only the cylinder was instrumented with pressure tappings and had seven streamwise rows of 20 tappings each at the circumferential stations  $\phi = 0^\circ, 30^\circ, 60^\circ, 90^\circ, 120^\circ, 150^\circ$  and  $180^\circ$ . The wall temperature was monitored using 3 chromel-alumel thermocouples installed in the cylinder.

Model 2 had separate cylindrical, ogive, and tip sections (P,R3 and F3 only) which could be fitted together using internal cylindrical guides and set-screws. The ogive and tips F3 and R3 were each instrumented with two streamwise rows of tappings  $180^\circ$  apart. Because of internal space constraints, tip P was not instrumented. By aligning the tap rows on the ogive and the tip and then rotating the assembly relative to the cylinder, pressure distributions along opposing  $\phi$  pairs ( $0^\circ - 180^\circ, 30^\circ - 210^\circ$ , etc.) were obtained.

Both models were secured in the tunnel using an axial sting downstream of the cylinder. A ball joint adapter, restricting motion to the vertical plane only, permitted angle of attack settings in the range  $-4.5^\circ \leq \alpha \leq 4.5^\circ$ .

### 2.3 Angle of Attack.

The position  $\alpha = 0^\circ$  was set iteratively. Several runs were made and  $\alpha$  was adjusted until pressure distributions along the rows  $\phi = 0^\circ, 90^\circ$ , and  $180^\circ$  were within  $\pm 1\%$  of each other. Inviscid calculations of  $P_w$  along  $\phi = 0^\circ$  and  $180^\circ$  indicated that a  $\pm 1\%$  variation corresponds to an accuracy in  $\alpha$  of  $\pm 0.2^\circ$ . Other values of  $\alpha$  were then set by displacing the tip a pre-computed distance. The additional error in doing so is estimated to be

$\pm 0.05^\circ$ . Prior to a run, the cross-wires of a telescopic sight were focused on the model tip. Vibration was observed on startup (and at shutdown), but during the test the model was steady at the same position as before startup.

#### 2.4 Measurements and Data Documentation.

The model configurations for which wall pressure distributions and pitot pressure surveys were obtained are listed in Tables 1 and 2 respectively. The data, in the form  $P_w$  ( $\text{Nm}^{-2}$ ) and  $P_w/P_\infty$  vs.  $X/D$  and  $P_t$  ( $\text{Nm}^{-2}$ ) and  $u$  (m/s) vs.  $y$  (m) are available in hard copy form or on a 9 track, 1600 bpi magnetic tape. Copies of both can be obtained from the first author.

The locations  $X/D = 3.26, 5.05$  and  $6.33$  at which the pitot surveys were made are referred to as stations 1, 2 and 3 respectively in the remainder of the text. Note that for the blunt tip models  $X/D$  is measured relative to the virtual (pointed) origin (Fig. 1).

The pitot probe tip was made of flattened tubing and had a height of  $0.18\text{mm}$  ( $0.007''$ ). Data taken less than  $1\frac{1}{2}$  probe heights above the wall were judged to be within the probe interference zone and were discarded. Velocity profiles were obtained from the pitot profiles assuming that: a)  $P(y) = P_w$ , b)  $T_o(y) = T_{o_\infty} [1 + 0.05(1-y/\delta)]$ . Assumption a) was verified

TABLE 1

Configuration	Pressure Distributions	$\alpha^\circ$	$\phi^\circ$
Model 1 All Tips	Cylinder Body	0,2.9	0 to 180 (30)
Model 2 Tip P	Ogive	0,1,2 2.9 4.45	0 and 180 0 to 180 (30) 0 and 180
Model 2 Tip R3	Ogive and Tip	0,1,2 2.9 4.45	0 and 180 0 to 180 (30) 0,30,60,120,150,180
Model 2 Tip F3	Ogive and Tip	0 1.5,2.9 4.45	0 and 180 0 to 180 (30) 0,30,150,180

TABLE 2

Configuration	$\alpha^\circ$	$\phi^\circ$	X/D
Model 1, All Tips	0 and 2.9	0 and 180	3.26, 5.05, 6.33

experimentally. Static pressure surveys at stations 1 and 2 using tip F3 showed that the maximum variation was  $\pm 2\%$ .

The velocity profiles were analyzed using a boundary layer code developed originally by Sun and Childs.<sup>15</sup> It uses an iterative technique to fit the data to the combined "law of the wall - law of the wake". The wall-wake parameters are varied until the deviation of the data from the combined law are minimized. In all cases, good fits were obtained. The values of  $\delta$ ,  $\delta^*$ ,  $\theta$ ,  $H$ ,  $C_f$  and  $\bar{A}$  given below are from this code. The overall accuracy of  $\delta^*$ ,  $\theta$ ,  $C_f$  and  $\bar{A}$  is estimated to be better than  $\pm 10\%$ .

### 3. Discussion of Results.

#### 3.1 Wall Pressures.

As indicated in Table 2, boundary layer surveys were made along  $\phi = 0^\circ$  and  $180^\circ$  for  $\alpha = 0^\circ$  and  $2.9^\circ$ . The streamwise pressure distributions in which these profiles develop are shown in Figure 2. Each data band includes results for the 7 tips and has a variation of about  $\pm 1.5\%$  about the mean value. No systematic effects of blunting are detectable within each band.

Pressure distributions on the ogive (for tips R3 and F3) at  $\alpha = 0^\circ$  are shown in Figure 3. For clarity, the data points near the tip are connected by straight lines. The exact positions of tips R3 and F3 are  $X/D = 0.309$  and  $0.404$  respectively. The tap positions on the tips are shown in the inset sketches. By  $X/D = 0.5$ , the distributions for the two cases are essentially coincident. Thus, the influence of blunting is confined to the tip itself and to a very short region downstream of the junction with the ogive. Data for tip P (which could not be obtained further upstream than  $X/D = 1.5$ ) are also shown in Figure 3. Agreement between the 3 data sets is good.

The pressures at taps 1' and 1 on tips R3 and F3 respectively are within 1% of  $P_{t_2}$ . For F3,  $P_w = P_{t_2}$  over most of the face, but in the strong expansion around the tip corner decreases below  $P_\infty$ . The subsequent recovery to the "ogive" value occurs through a conical recompression shock wave (Fig. 4a). Here, "ogive" value refers to the pressure measured

using tip P. In studies at  $M_\infty = 2.3$ , the same geometry tip was tested and similar shock patterns were reported.<sup>1,12</sup> No recompression shocks were observed with the R series tips. The shock pattern obtained for R3 (Fig. 4b) is typical of the 3 cases tested (note: the weak compression indicated by the arrow is caused by a very small step, 5 $\mu$ m high, where the tip and ogive sections join).

Distributions for tips F3 and P at  $\alpha = 2.9^\circ$  are shown in Figure 5. For clarity, data for R3 are not shown. Except on the tip itself, they agree well with the results for F3 and P. With F3, the windside recompression shock moves upstream and increases in strength, whereas the opposite occurs on the leeside. The shadow photograph confirms this (Fig. 4c). For R3, a series of interior shocks occurs on the ogive windside (Fig. 4d). They are very weak and have no measurable effect on  $P_w$ . Similar patterns were seen with tips F1 and R2. It has been suggested that these waves result from the reflection of expansion waves (downstream of the sonic point) from the bow shock and sonic line which are then reflected from the body.<sup>16</sup> The fact that this process would be highly geometry dependent is a plausible explanation of why it can appear and then disappear with small changes in tip shape.

Summarizing,  $P_w$  recovers rapidly to the "ogive" value, even with significant blunting.  $X_{ew}$ , the distance for completion of entropy wake effects on the pressure distribution, is small. For the cases tested here,  $X_{ew}/D \leq 0.7$ . In the absolute sense, the different growth rates of  $\delta^*$  generated by different tips will cause small differences in  $P_w$  along the body. The differences are well within the normal range of experimental scatter and, consequently, are not detectable.

### 3.2 Boundary Layer Properties.

#### 3.2.1 $\alpha = 0^\circ$ .

It is well known that tip bluntness and  $\alpha$  influence the transition location.<sup>17</sup> In this study, the latter was deduced from shadow photographs and is, therefore, only qualitative and indicative of general trends. For tip P,  $(S/D)_{tr} \sim 0.9 - 1.5$ . With the R series tips, the higher entropy, lower Mach number fluid adjacent to the surface delays transition. In contrast, transition for the F series tips occurs earlier than with tip P and is in the range  $0.7 \leq (S/D)_{tr} \leq 1.1$ . The reason for this is not entirely clear, but it is possible that the recompression shock wave acts as a "trip" which overcomes the delaying influence of the higher entropy, lower Mach number fluid generated by the bow shock.

Velocity profiles are shown in Figure 6. For clarity, only four profiles are shown at each station.  $y$  and  $u$  are normalized by  $D$  and  $U_\infty$  respectively, rather than  $\delta$  and  $U_e$  in order to highlight the effects on the profile shape and thickness. At all stations, blunting retards the profile and increases its thickness. The latter is caused mainly by the

progressively larger entropy wake associated with increased blunting and not from growth of the boundary layer proper. Although  $y_e$  is difficult to define precisely for tips R3 and F3, the region where the boundary layer profile turns upward and merges with the entropy wake is discernible.

Values of  $n$  obtained from least-squares curve fits to the power law approximation  $\frac{u}{U_e} = \left(\frac{y}{\delta}\right)^{1/n}$  are shown versus  $Re_\theta$  in Figure 7a. The hatched band brackets data for about 80 profiles from four different zero-pressure-gradient studies.<sup>18</sup> The expansion over the ogive generates fairly full profiles at station 1 ( $n = 5.9 - 6.9$ ). Over the upstream section of the cylinder  $dP/dx$  is positive and decreases  $n$  to the range 5.6 - 6.0, then as  $dP/dx \rightarrow 0$  with increasing  $X/D$ ,  $n$  increases. The distance required for  $n$  to recover to values within the hatched band is a strong function of tip bluntness. For P and R1, the recovery is complete by station 3. For R3, linear extrapolation indicates recovery at  $X/D \approx 20-30$ , whereas for F3 the recovery has not even begun by station 3.

The influence of different tips on  $n$  (and on other profile and integral parameters) can be correlated when plotted in terms of a bluntness length,  $B$ , given by

$$B = \int_0^{\theta_d} \delta_s ds \quad (\text{see inset, Figure 7b}) \quad (1)$$

At  $\alpha = 0^\circ$ , the values of  $B$  (in mm.) are given in Table 3. It is seen that, in terms of increasing  $B$ , the different geometry tips occur in alternate order. Figure 7b shows  $n$  as a function of  $B/D$ . By station 3 there is a consistent trend of decreasing  $n$  with increasing  $B/D$ . Viewed simply, this reflects the "shorter history" caused by the Reynolds number reduction which occurs with increased blunting.

The additional pressure drag,  $Dp_b$ , due to tip bluntness, can also be used as a correlating parameter. Both  $Dp_b$  and  $B$  give similar data correlations.<sup>6</sup> The utility of  $B$  is that it can be calculated easily, given the tip geometry and  $M_\infty$ .

The development of  $\delta^*$  and  $\Theta$  is shown in Figure 8. For clarity in this and subsequent figures, the data points are joined by straight lines. Values of  $H$  and  $\bar{\Lambda}$  are given in Table 3. At any station,  $H$  is approximately constant up to a critical value of blunting,  $B_c$ , and then decreases.  $B_c$  increases with  $X/D$ , reflecting the progressive dissipation of entropy wake effects. At station 3, only the bluntest tips (R3 and F3) influence  $H$ .

Although  $H$  is approximately constant for  $B < B_c$ ,  $\delta^*$  and  $\Theta$  are influenced significantly by small amounts of blunting. Their detailed behavior with  $B$  is complex and depends on  $X/D$ . However, with increasing  $X/D$  a consistent trend emerges. As shown in Figures 9a and 9b, by station 3 ( $X/D = 6.33$ ), both  $\delta^*$  and  $\Theta$  increase with increasing  $B/D$ .

TABLE 3

B(mm)	TIP	H			$\bar{\Lambda}$		
		St.1	St.2	St.3	St.1	St.2	St.3
0	P	5.26	5.21	5.08	0.55	0.77	0.57
1.34	R1	5.38	5.26	5.07	0.67	0.85	0.60
1.99	F1	5.39	5.22	5.08	0.57	0.78	0.71
3.33	R2	5.16	5.13	5.09	0.66	0.82	0.76
4.99	F2	5.11	5.11	5.06	0.79	0.98	0.89
6.58	R3	4.51	4.72	4.80	0.61	0.92	0.88
9.97	F3	4.05	4.16	4.43	0.51	0.82	0.98

$C_f$  as a function of  $X/D$  is shown in Figure 10a. At any station, blunting initially decreases  $C_f$ , but beyond a certain value it increases. At the upstream stations, only tips R3 and F3 generate values greater than that for tip P. The results at station 3 are qualitatively similar, but the increase after the initial decrease is much smaller so that  $C_f$  for all blunt tips is below, but within 10%, of the value for P. Further, other than for R3 at station 1 and F3 at stations 1 and 2, the data correlate reasonably well with  $Re_\theta$  (Fig. 10b). The weak adverse pressure gradient causes  $C_f$  to fall below the zero-pressure-gradient Van Driest II prediction,<sup>19</sup> shown by the solid line, but the discrepancy is typically less than 10%.

$\bar{\Lambda}$  is strongly influenced by tip blunting (Table 3). In all cases, the adverse pressure gradient causes an increase from stations 1 to 2. Except for F3,  $\bar{\Lambda}$  then decreases as the pressure gradient relaxes. Small amounts of blunting have a significant effect on  $\bar{\Lambda}$ , even 6 calibers from the tip. At this station, only tips P and R1 have values of  $\bar{\Lambda}$  within the accepted range for zero-pressure-gradient turbulent boundary layers. With increased blunting,  $\bar{\Lambda}$  increases and, as shown in Figure 9c, correlates reasonably well with  $B/D$ .

In summary, the effects of tip bluntness on the inner part of the profile (as reflected in  $C_f$ ) dissipate in a fairly short streamwise distance from the tip. The effects on the outer region, which are much more directly affected by the entropy wake, require significantly larger distances.

### 3.2.2 $\alpha = 2.9^\circ$

$\delta^*$  and  $\Theta$  along  $\phi = 0^\circ$  and  $180^\circ$  are plotted in Figures 11 and 12 respectively. On the leeside, the combination of the stronger adverse  $dP/dx$  and the crossflow increases the magnitudes and growth rates of both quantities by a factor of 2 or more over their values at  $\alpha = 0^\circ$ . On the windside, both the absolute values and growth rates are lower. On the

leeside the effects of blunting are the same at all stations, whereas on the windside the effects depend on position.  $H$  versus  $B/D$  is shown in Figure 13. The effects of blunting are greater on the leeside. The windside trends are the same as at  $\alpha = 0^\circ$ , except that the weaker  $dP/dx$  results in a more rapid dissipation of entropy wake effects. At station 1, only the bluntest tips (R3 and F3) influence  $H$ . By station 3,  $H$  for all 7 tips is within 2% of the mean value and the trend of decreasing  $H$  for  $B > B_c$  is barely detectable. The opposite is true on the leeside. At station 1, even tips R1 and F1 noticeably influence  $H$ .  $B_c$  does increase with  $X/D$ , but less rapidly than on the windside or at  $\alpha = 0^\circ$ .

$n$  versus  $Re_\theta$  is shown in Figure 14a. The zero pressure gradient data band is again shown for comparison. On the windside, the weak adverse  $dP/dx$  and favorable  $dP/d\phi$  induce crossflow away from  $\phi = 0^\circ$ , generating full profiles. Since  $d\theta/dx$  is small (Fig. 12), this causes large values of  $n$  at low values of  $Re_\theta$ . In contrast, on the leeside, the stronger adverse  $dP/dx$  between stations 1 and 2 retards the profiles. This decreases  $n$  but increases  $\theta$  and  $d\theta/dx$ . Thus, by station 2, all profiles have low values of  $n$  but high values of  $Re_\theta$ . As  $dP/dx$  relaxes, the expected trend of increasing  $n$  with increasing  $Re_\theta$  is seen in all cases.

$C_f$  on the wind- and leesides is shown in Figures 14b and 14c respectively. At a given station and with a given tip, the stronger adverse  $dP/dx$  along  $\phi = 180^\circ$  results in lower values of  $C_f$  than along  $\phi = 0^\circ$ . For all tips,  $C_f$  decreases with  $X/D$ , more rapidly on the leeside than windside. Downstream of station 1, which is affected by expansion over the ogive, the data correlate reasonably well with  $Re_\theta$ . On the windside, where  $dP/dx$  is only mildly adverse, the agreement with the zero-pressure-gradient Van Driest II prediction is good. On the leeside, the stronger adverse  $dP/dx$  results in values about 20% below the prediction.

In general, at a given station,  $C_f$  increases with increased blunting. On the windside, the influence of blunting dissipates rapidly. At station 1,  $C_f$  for tips P, R1, F1, R2 and F2 is within 4% of the mean value. Tips R3 and F3 are 11% and 21% respectively above the mean. By station 2,  $C_f$  for all tips is within 3% of the mean value and no systematic influence of  $B$  is detectable. In contrast, on the leeside, the range of  $C_f$  at a given station increases with  $X/D$ . At station 1,  $C_f$  for P, R1, F1, R2 and F2 are all within 1% of the mean value, with R3 and F3 20% and 28% respectively above the mean. However, at station 3,  $C_f$  decreases from 0.00107 to .00092 as  $B/D$  increases from 0 to 0.1 then increases to 0.00131 as  $B/D$  increases to its maximum.

$\bar{\Lambda}$  versus  $B/D$  is shown in Figure 15. For a given tip (except F3), the windside values of  $\bar{\Lambda}$  decrease with  $X/D$ . At station 3 (where  $dP/dx \approx 0$ ),  $\bar{\Lambda}$  is in the range 0.22-0.34, substantially below the  $\alpha = 0^\circ$  case (Table 3). On the leeside,  $\bar{\Lambda}$  increases by a factor

of 2 or more from station 1 to 2 but between stations 2 and 3 typically changes less than 5%. The trend with  $B$  is consistent from station to station; intermediate values of  $B$  increase  $\bar{A}$ , but a large amount of blunting decreases it to the pointed value.

Overall, the effects of small  $\alpha$  on the wind- and leeside boundary layers are qualitatively similar for all tips. However, as  $B$  increases, the detailed behavior of a given parameter at a fixed station is generally complex, particularly at the upstream stations where the combined influences of the different starting conditions, transition location, and the external entropy wake interact strongly.

#### 4. Concluding Remarks

An experimental study has been made of the effects of nose tip blunting on the surface pressure distribution and the wind- and leeside boundary layer development on a tangent-ogive cylinder model. The tests were made at small angles of attack ( $0 - 4.5^\circ$ ) in a high Reynolds number, Mach 3 airflow under approximately adiabatic wall temperature conditions. Models with pointed, tangent-hemisphere and flat-faced nose tips were tested. The results show that:

(i) The distance for completion of entropy wake effects on the surface pressure distributions is small. Even with significant tip blunting, the effects are confined to the tip itself and a short region downstream of the junction with the ogive.

(ii) The bow shock generated by a blunt tip not only creates an entropy wake but also affects both the initial conditions for boundary layer growth and transition. Hence, tip bluntness has a strong influence on the development of all boundary layer properties. Since each of these properties has a different sensitivity to tip blunting, the streamwise station at which the effects of blunting can be considered complete is a function of the particular property selected.

(iii) The effects of different tip shapes can be correlated in terms of a bluntness length  $B$ .  $B$  is obtained by integrating the local tip surface angle from the stagnation point to the point corresponding to shock wave detachment. At stations close to the ogive shoulder, the interaction of the three factors given above generally results in a complex relationship between any property and  $B$ . Further downstream, simpler trends with  $B$  are observed and good correlations can be obtained.

(iv) The effects of angle of attack are qualitatively similar for all tips. In general, entropy wake effects dissipate more rapidly in the near-zero pressure gradient on the windside than on the leeside, which has a stronger adverse pressure gradient. The effects of different tip shapes can also be correlated as a function of  $B$ .

### Acknowledgements

This work was supported by the Army Research Office under grants DAAG 29-84-M-0432 and DAAG 29-77-G-0234 monitored by Dr. R. Singleton. The experimental phase of the study was carried out at the Gas Dynamics Laboratory of Princeton University. Many helpful discussions with Professors S. M. Bogdonoff and G. S. Settles are gratefully acknowledged.

### References

1. Sturek, W.B., "Application of CFD to the Aerodynamics of Spinning Shell," AIAA Paper 84-0323, 22nd Aerospace Sciences Meeting, Jan. 1984.
2. Sturek, W.B., "Preliminary Surveys of the Three Dimensional Boundary Layer on a Yawed Spinning Body of Revolution," BRL-MR-2501, July 1975.
3. Sturek, W.B. and Reba, J.J., "Measurements of Wall Static Pressure on a Yawed Tangent Ogive Cylinder Model," BRL-MR-2699, Nov. 1976.
4. Sturek, W.B. and Danberg, J.E., "Experimental Measurements of the Turbulent Boundary Layer on a Yawed, Spinning Slender Body," BRL-R-1954, Jan. 1977.
5. Reklis, R.P. and Sturek, W.B., "Surface Pressure Measurements on Slender Bodies at Angle of Attack in Supersonic Flow," U.S. Army Ballistic Research Laboratory ARBRL-MR-02876, Nov. 1978.
6. Gray, W.K., "An Experimental Investigation of Tip Bluntness Effects on the Turbulent Compressible Boundary Layer on an Axisymmetric Body," Mechanical and Aerospace Engineering Department, Princeton University Thesis 1495-T, March 1981.
7. Kayser, L.D. and Sturek, W.B., "Experimental Measurements in the Turbulent Boundary Layer of a Yawed, Spinning Ogive-Cylinder Body of Revolution at Mach 3. Part I. Description of the Experiment and Data Analysis," ARBRL-MR-02808, Jan. 1978.
8. Kayser, L.D., Yanta, W.J., and Sturek, W.B., "Measurements in the Turbulent Boundary Layer of a Yawed, Spinning Body of Revolution at Mach 3.0 with a Laser Velocimeter and Impact Probe," Technical Report ARBRL-TR-02074, May 1978.
9. Kayser, L.D. and Sturek, W.B., "Turbulent Boundary Layer Measurements on the Boattail Section of a Yawed, Spinning Projectile Shape at Mach 3.0," U.S. Army Ballistic Research Laboratory ARBRL-MR-02880, Nov. 1978.
10. Nietubicz, C.J., Inger, G.R., and Danberg, J.E., "A Theoretical and Experimental Investigation of a Transonic Projectile Flow Field," AIAA Paper 82-0101, 20th Aerospace Sciences Meeting, Jan. 1982.
11. Reklis, R.P., Danberg, J.E., and Inger, G.R., "Boundary Layer Flows on Transonic Projectiles," AIAA Paper 79-1551, 12th Fluid and Plasma Dynamics Conference, June 1979.

12. Sturek, W.B., Guidos, B., and Nietubicz, C.J., "Navier-Stokes Computational Study of the Magnus Effect on Shell with Small Bluntness at Supersonic Speeds," AIAA Paper 82-1341, 9th Atmospheric Flight Mechanics Conference, Aug. 1982.
13. Stetson, F., "Nose Tip Bluntness Effects on Cone Frustrum Boundary Layer Transition in Hypersonic Flow," AIAA Paper 83-1763, 16th Fluid and Plasma Dynamics Conference, July 1983.
14. Dolling, D.S. and Gray, W.K., "Compilation of Wall Pressure and Turbulent Boundary Layer Data for Supersonic High Reynolds Number Flow over a Blunted Tangent Ogive Cylinder at Small Angles of Attack," Gas Dynamics Laboratory Report #1585-MAE, Princeton University, Sept. 1982.
15. Sun, C.C. and Childs, M.E., "A Modified Wall-Wake Velocity Profile for Turbulent Compressible Boundary Layers," AIAA Journal of Aircraft, Vol. 10, June 1973, pp. 381-383.
16. Perkins, E.W., Jorgensen, L.H., and Sommer, S.C., "Investigation of the Drag of Various Axially Symmetric Nose Shapes of Fineness Ratio 3 for Mach Numbers from 1.24 to 7.4," NACA Report 1386, 1958.
17. Ericsson, L.E., "Correlation of Attitude Effects on Slender Vehicle Transition," AIAA Journal, Vol. 12, April 1974, pp. 523-529.
18. Settles, G.S. and Bogdonoff, S.M., "Separation of a Supersonic Turbulent Boundary Layer at Moderate to High Reynolds Numbers," AIAA Paper 73-666, 6th Fluid and Plasma Dynamics Conference, July 1973.
19. Hopkins, E.J., "Charts for Predicting Turbulent Skin Friction from the Van Driest Method (II)," NASA TN-D-6945, Oct. 1972.

Publications/Participating Personnel

- a) Publications: D. S. Dolling and W. K. Gray, "Experimental Study of the Supersonic Turbulent Boundary Layer on a Blunted Axi-Symmetric Body" (accepted for publication by AIAA Journal).
- b) Personnel: Dr. D. S. Dolling. No advanced degrees were awarded during the duration of the project.

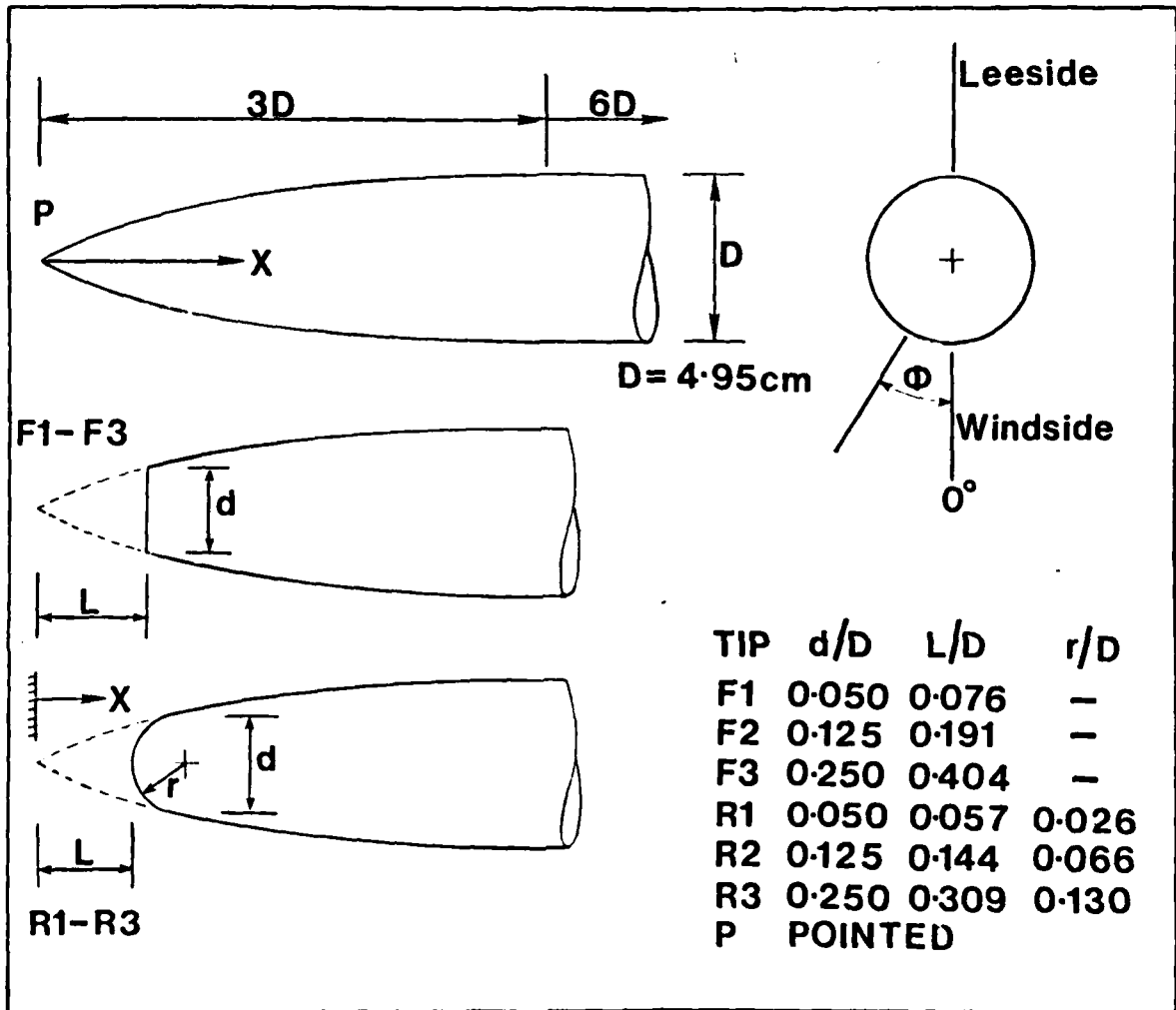


Figure 1. Models and Coordinate System

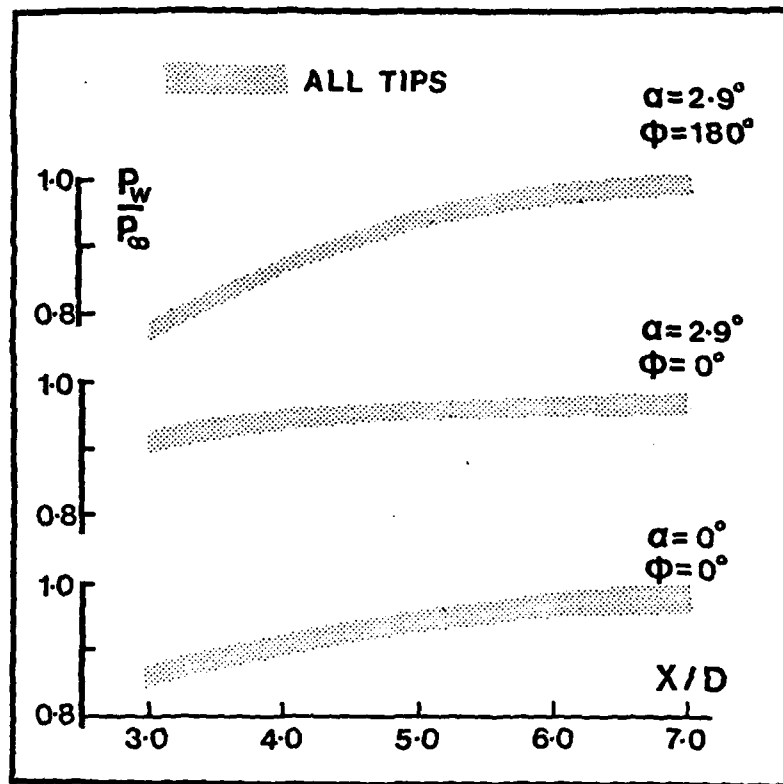


Figure 2. Pressure Distributions on Cylinder Body

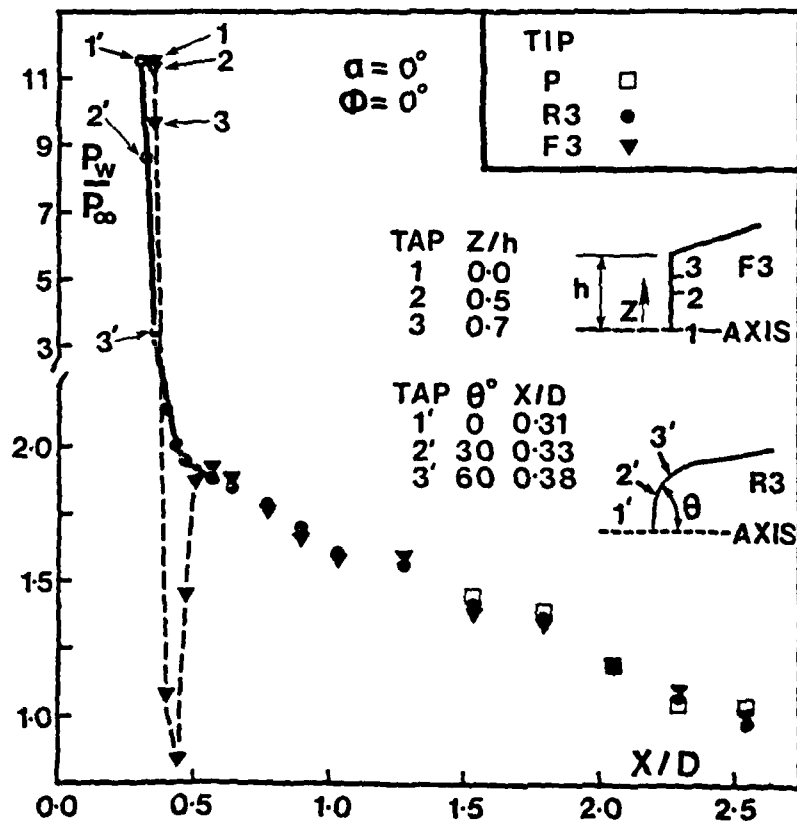


Figure 3. Pressure Distribution on the Ogive and Tip ( $\alpha = 0^\circ$ )

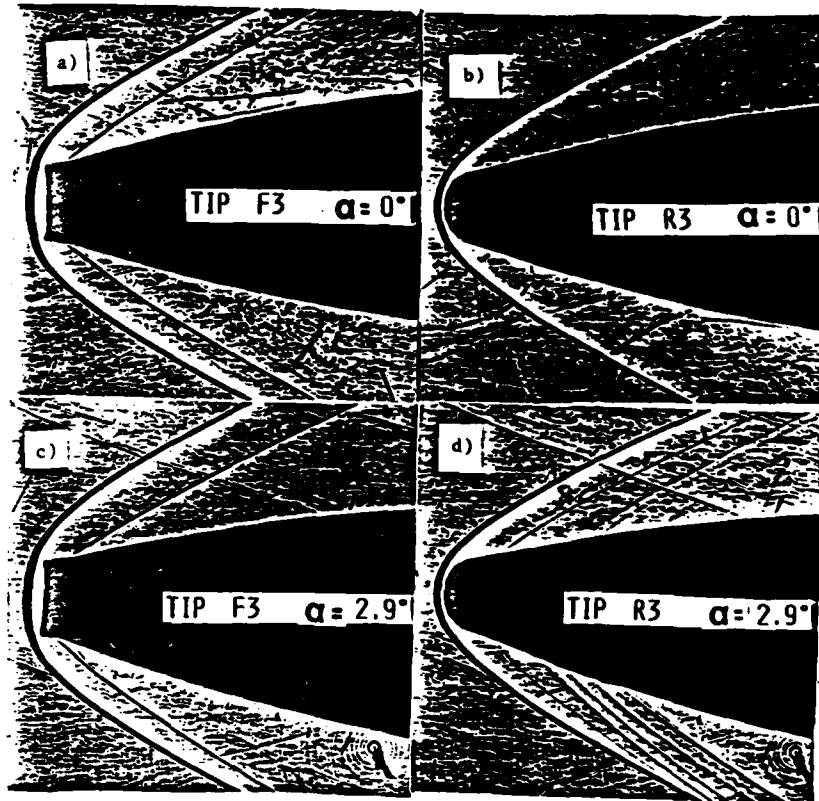


Figure 4. Shadow Photographs Using Tips R3 and F3

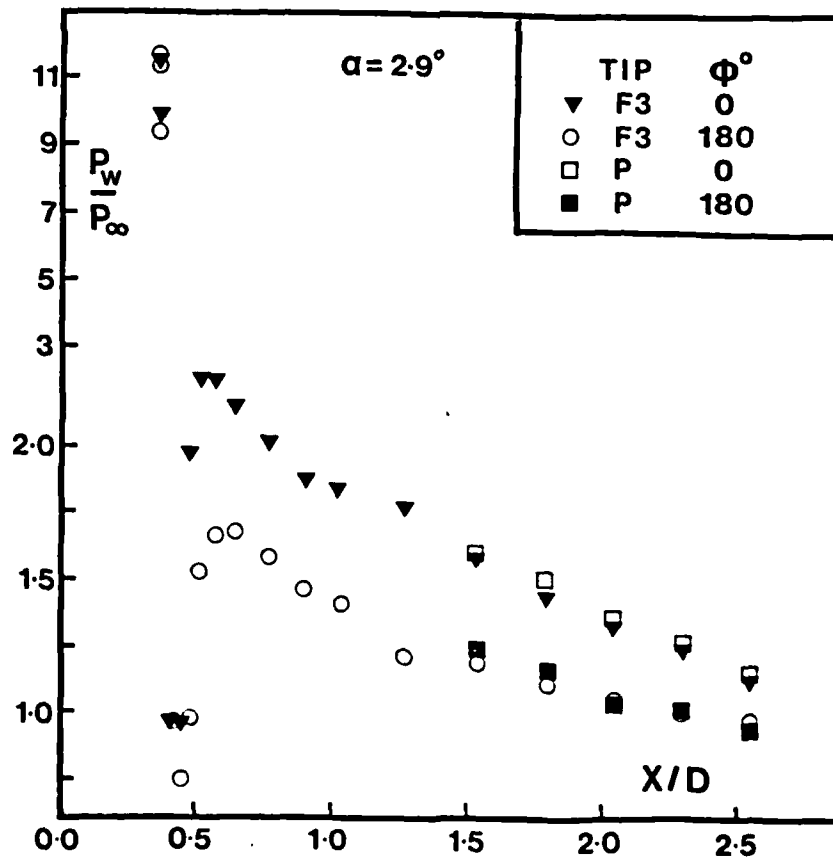


Figure 5. Pressure Distributions on the Ogive and Tip ( $\alpha = 2.9^\circ$ )

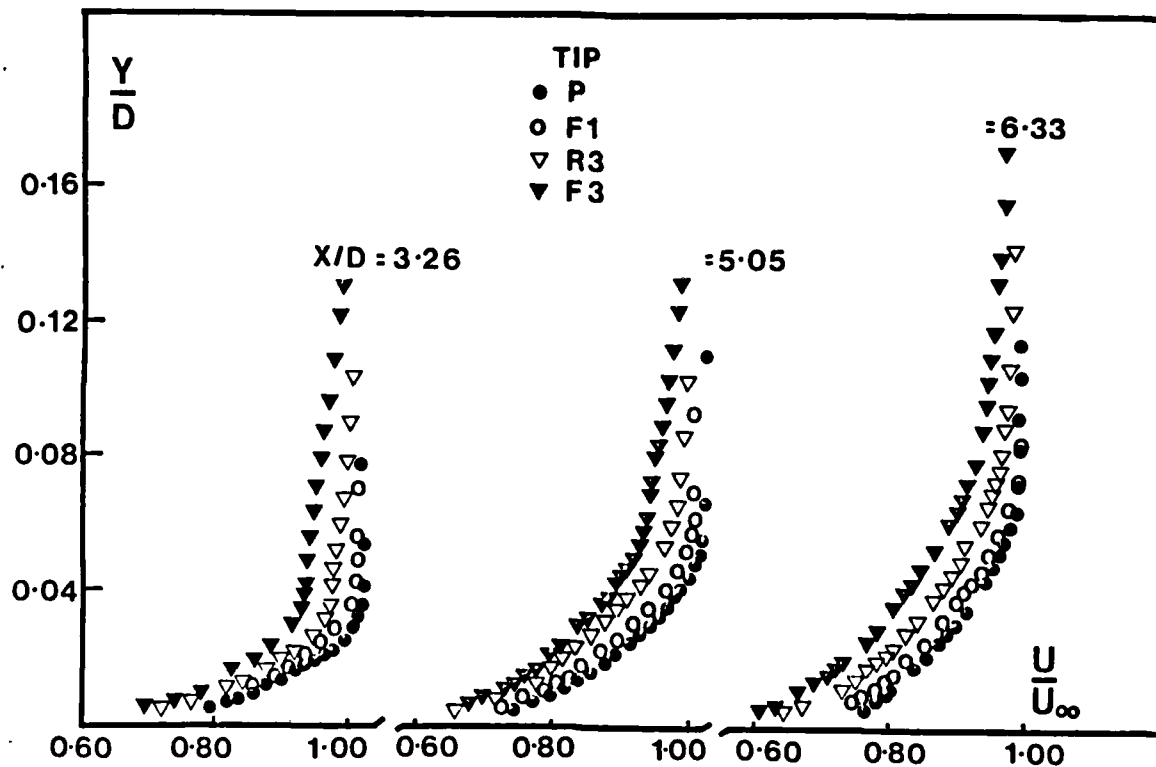


Figure 6. Boundary Layer Velocity Profile Development ( $\alpha = 0^\circ$ )

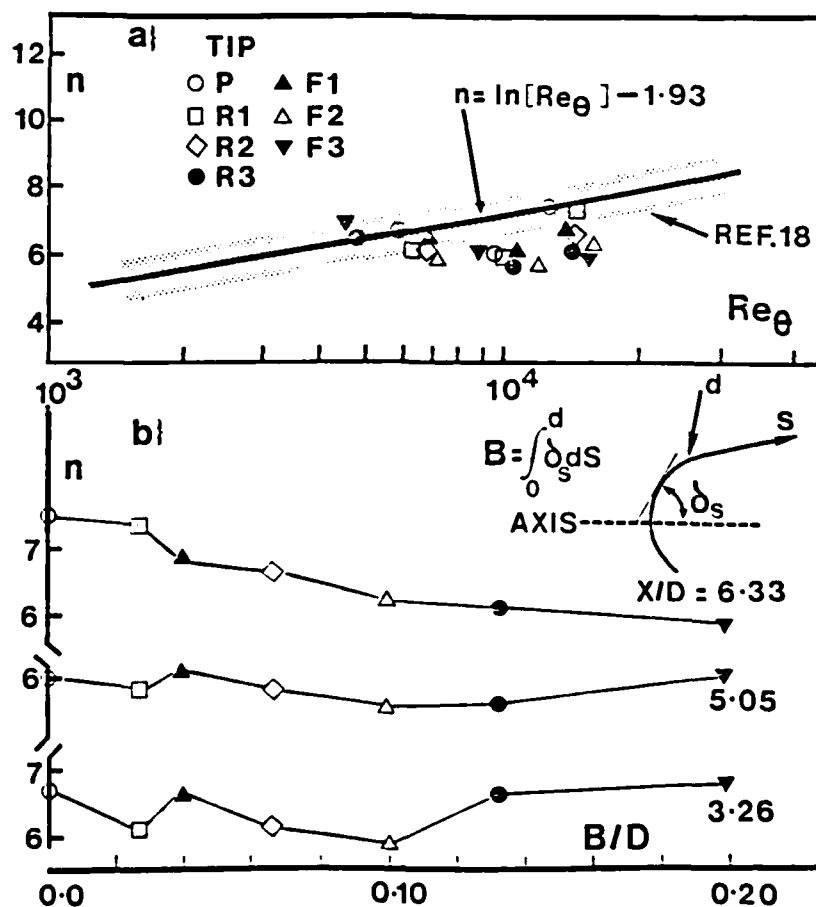


Figure 7. Boundary Layer Power Law Exponent  $n$  as a Function of  $Re_\theta$  and  $B/D$

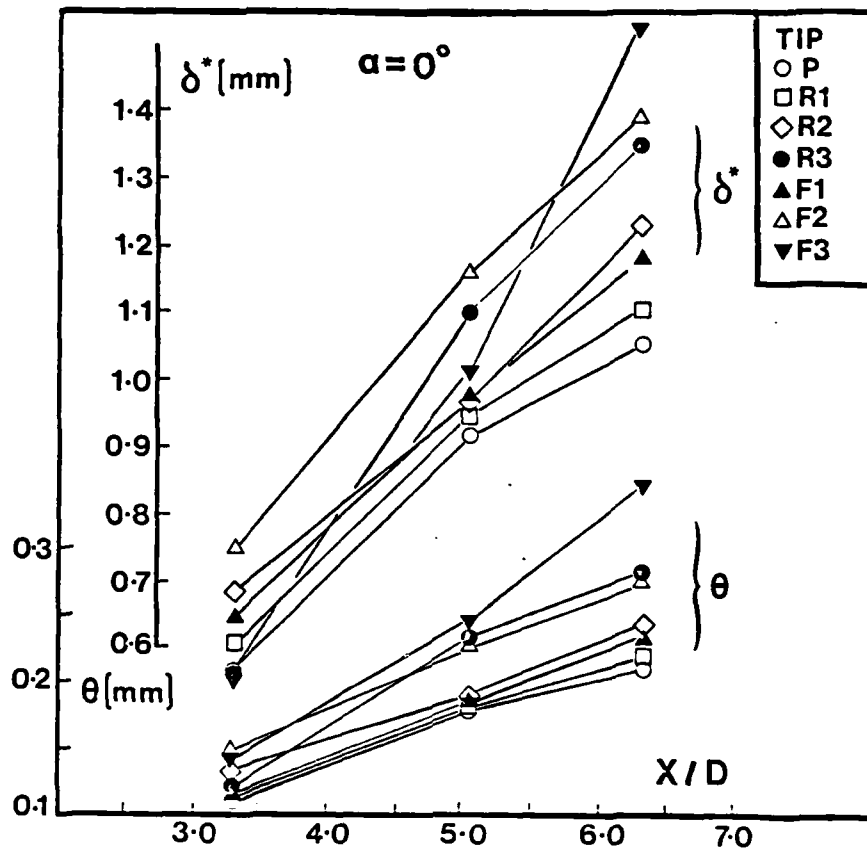


Figure 8. Streamwise Development of  $\delta^*$  and  $\theta$  ( $\alpha = 0^\circ$ )

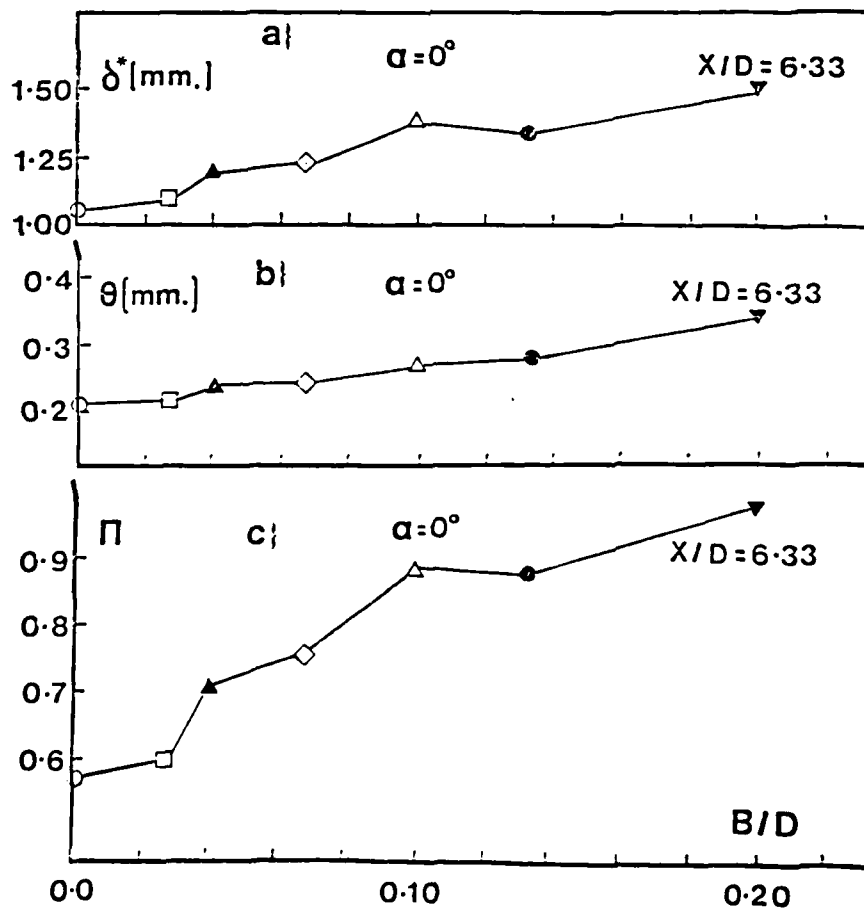


Figure 9. Correlation of,  $\delta^*$ ,  $\theta$  and  $\bar{\Pi}$  with  $B/D$  at Station 3 ( $\alpha = 0^\circ$ )

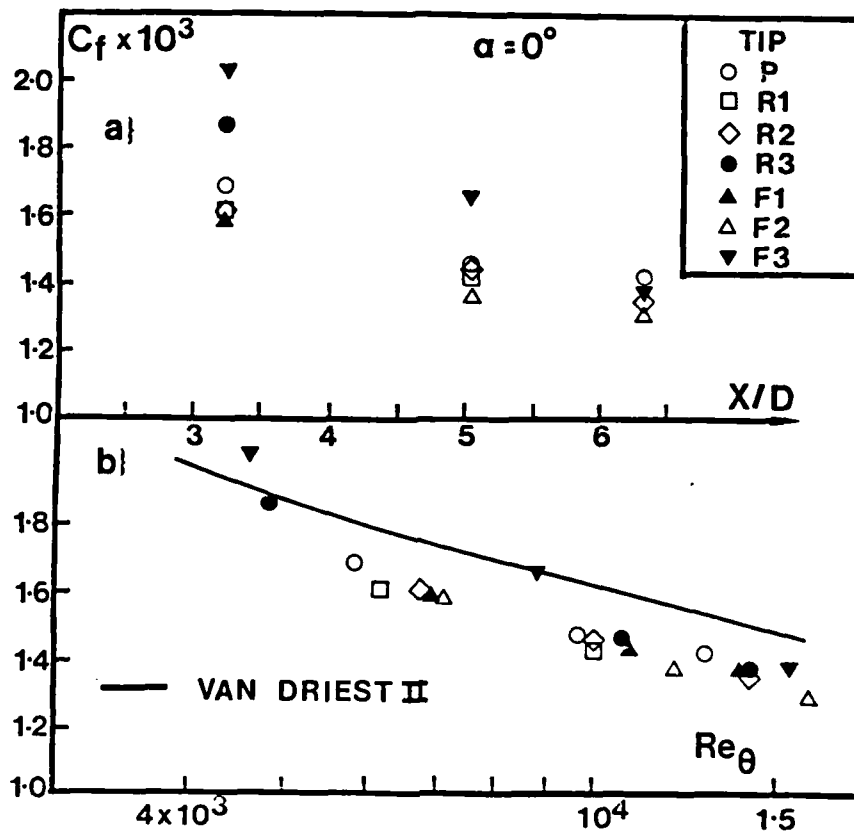


Figure 10. Skin Friction Coefficient as a Function of  $X/D$  and  $Re_\theta$

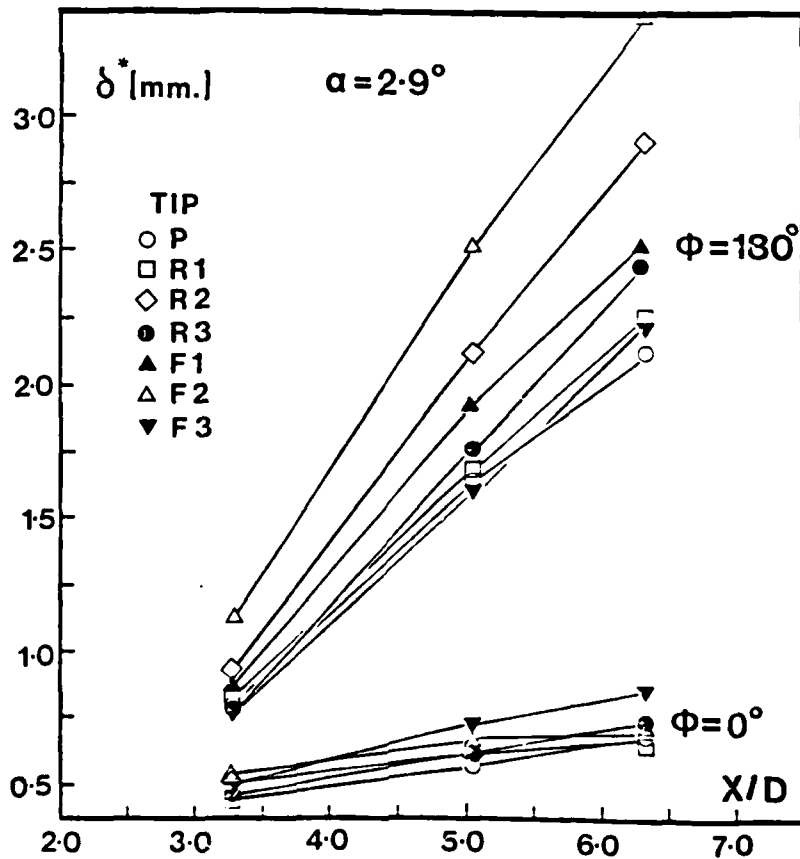


Figure 11. Wind and Leeside Development of  $\delta^*$  ( $\alpha = 2.9^\circ$ )

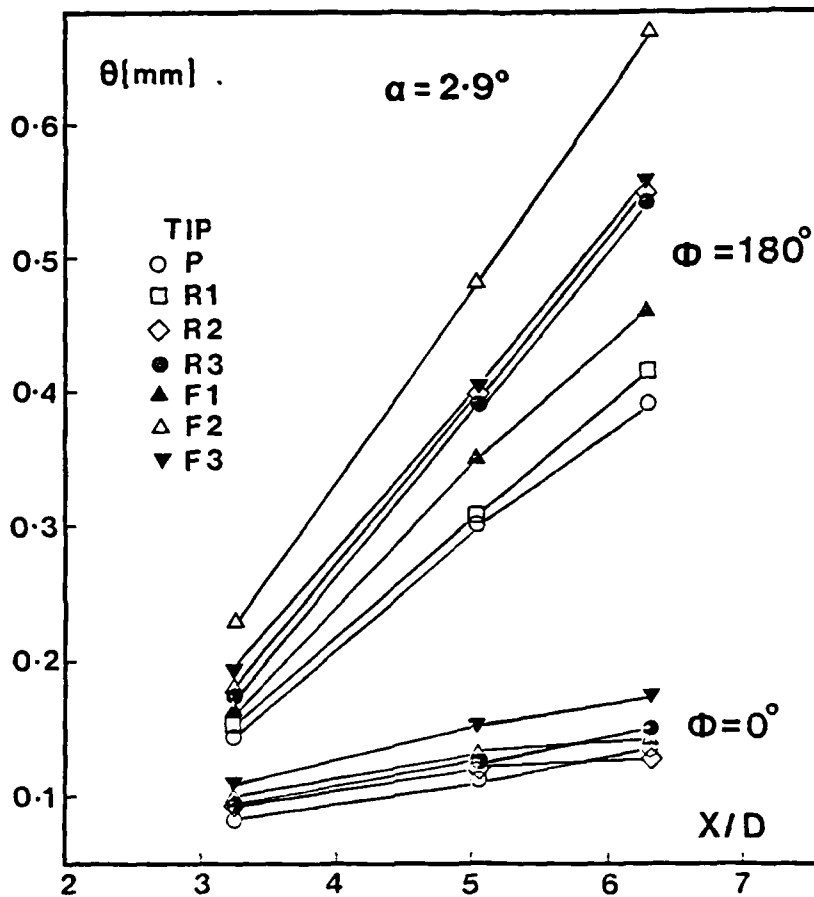


Figure 12. Wind and Leaside Development of  $\theta$  ( $\alpha = 2.9^\circ$ )

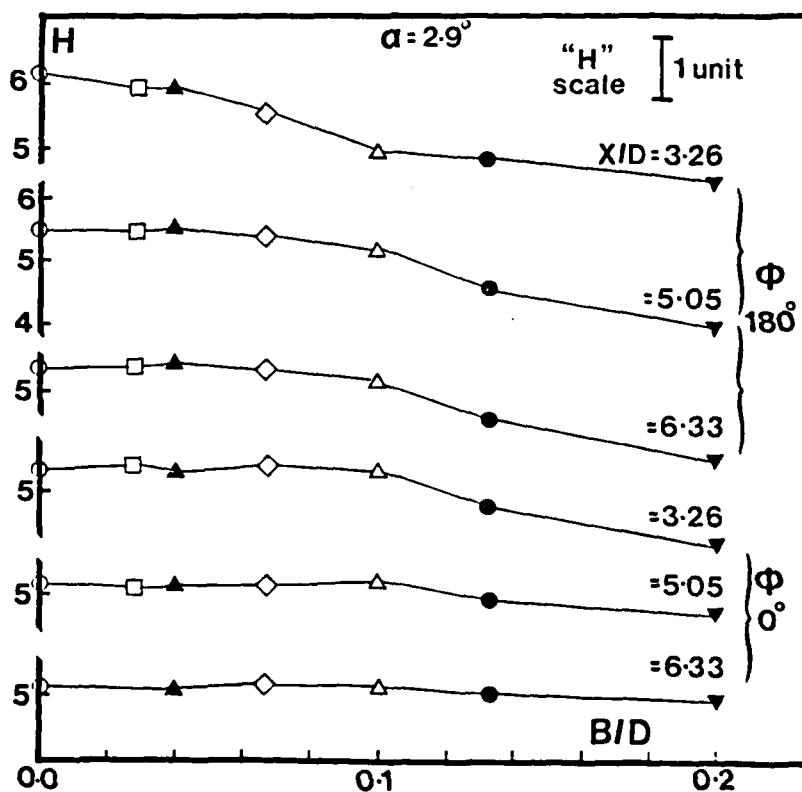


Figure 13. Boundary Layer Shape Factor as a Function of  $B/D$  ( $\alpha = 2.9^\circ$ )

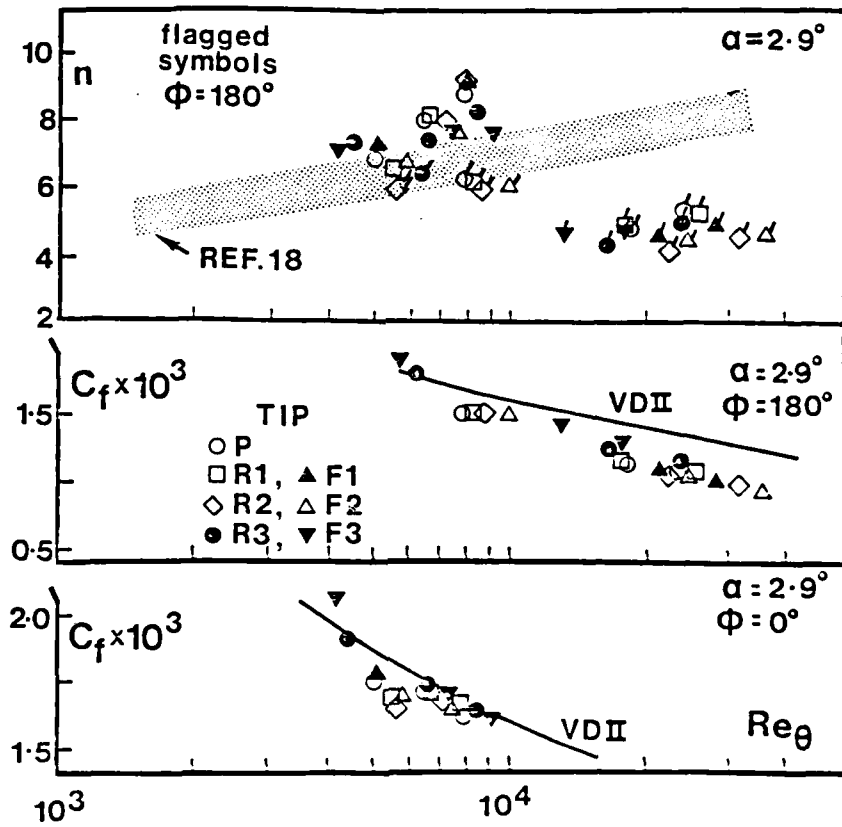


Figure 14. Velocity Profile Power Law Exponent and Skin Friction Coefficient as a Function of  $Re_\theta$  ( $\alpha = 2.9^\circ$ )

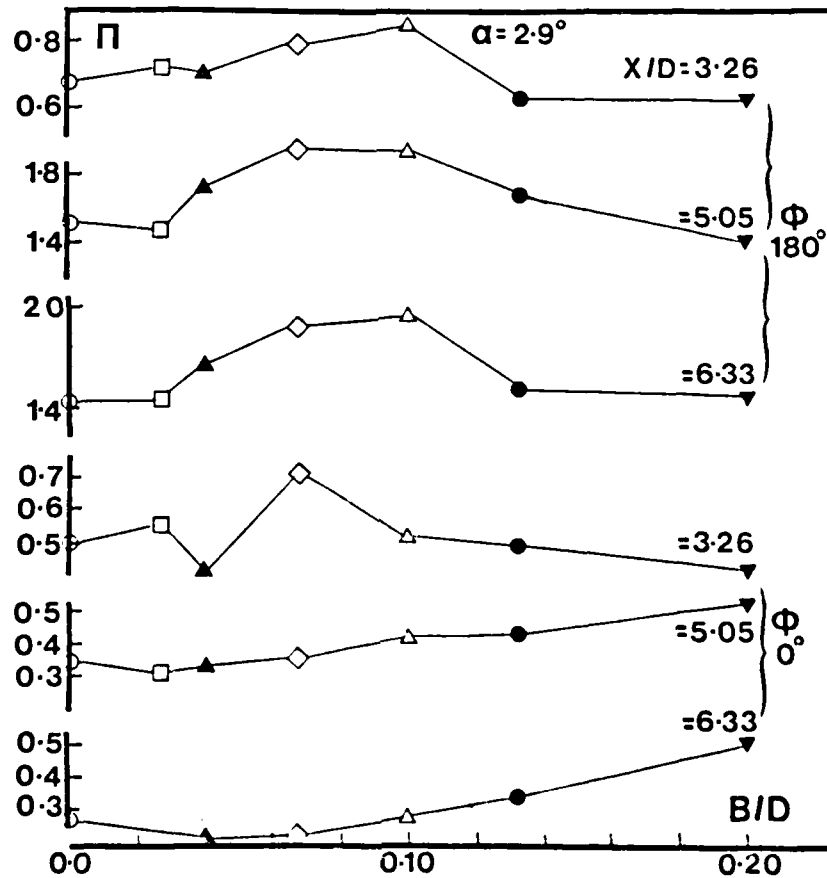


Figure 15. Wake Strength Parameter as a Function of  $B/D$  ( $\alpha = 2.9^\circ$ )

**END**

**FILMED**

3-86

**DTIC**